

Measurement of the cross-section ratio $\sigma_{\psi(2S)}/\sigma_{J/\psi(1S)}$ in deep inelastic exclusive ep scattering at HERA

ZEUS Collaboration

Abstract

The exclusive deep inelastic electroproduction of $\psi(2S)$ and $J/\psi(1S)$ at an ep centre-of-mass energy of 317 GeV has been studied with the ZEUS detector at HERA in the kinematic range $2 < Q^2 < 80 \text{ GeV}^2$, $30 < W < 210 \text{ GeV}$ and $|t| < 1 \text{ GeV}^2$, where Q^2 is the photon virtuality, W is the photon-proton centre-of-mass energy and t is the squared four-momentum transfer at the proton vertex. The data for $2 < Q^2 < 5 \text{ GeV}^2$ were taken in the HERA I running period and correspond to an integrated luminosity of 114 pb^{-1} . The data for $5 < Q^2 < 80 \text{ GeV}^2$ are from both HERA I and HERA II periods and correspond to an integrated luminosity of 468 pb^{-1} . The decay modes analysed were $\mu^+\mu^-$ and $J/\psi(1S)\pi^+\pi^-$ for the $\psi(2S)$ and $\mu^+\mu^-$ for the $J/\psi(1S)$. The cross-section ratio $\sigma_{\psi(2S)}/\sigma_{J/\psi(1S)}$ has been measured as a function of Q^2 , W and t . The results are compared to predictions of QCD-inspired models of exclusive vector-meson production.

The ZEUS Collaboration

H. Abramowicz^{26,v}, I. Abt²¹, L. Adamczyk⁸, M. Adamus³², S. Antonelli², V. Aushev^{16,17,p},
Y. Aushev^{17,p,q}, O. Behnke¹⁰, U. Behrens¹⁰, A. Bertolin²³, I. Bloch¹¹, E.G. Boos¹⁵,
K. Borras¹⁰, I. Brock³, N.H. Brook³⁰, R. Brugnera²⁴, A. Bruni¹, P.J. Bussey¹², A. Caldwell²¹,
M. Capua⁵, C.D. Catterall³⁴, J. Chwastowski⁷, J. Ciborowski^{31,x}, R. Ciesielski^{10,f},
A.M. Cooper-Sarkar²², M. Corradi¹, F. Corriveau¹⁸, R.K. Dementiev²⁰, R.C.E. Devenish²²,
G. Dolinska¹⁰, S. Dusini²³, J. Figiel⁷, B. Foster^{13,l}, G. Gach^{8,d}, E. Gallo^{13,m}, A. Garfagnini²⁴,
A. Geiser¹⁰, A. Gizhko¹⁰, L.K. Gladilin²⁰, Yu.A. Golubkov²⁰, J. Grebenyuk¹⁰, I. Gregor¹⁰,
G. Grzelak³¹, O. Gueta²⁶, M. Guzik⁸, W. Hain¹⁰, D. Hochman³³, R. Hori¹⁴, Z.A. Ibrahim⁶,
Y. Iga²⁵, M. Ishitsuka²⁷, A. Iudin^{17,q}, F. Januschek^{10,g}, N.Z. Jomhari⁶, I. Kadenko¹⁷,
S. Kananov²⁶, U. Karshon³³, M. Kaur⁴, P. Kaur^{4,a}, D. Kisielewska⁸, R. Klanner¹³,
U. Klein^{10,h}, N. Kondrashova^{17,r}, O. Kononenko¹⁷, Ie. Korol¹⁰, I.A. Korzhavina²⁰,
A. Kotański⁹, U. Kötz¹⁰, N. Kovalchuk¹³, H. Kowalski¹⁰, B. Krupa⁷, O. Kuprash¹⁰,
M. Kuze²⁷, B.B. Levchenko²⁰, A. Levy²⁶, V. Libov¹⁰, S. Limentani²⁴, M. Lisovyi^{10,i},
E. Lobodzinska¹⁰, B. Löhr¹⁰, E. Lohrmann¹³, A. Longhin^{23,u}, D. Lontkovskiy¹⁰,
O.Yu. Lukina²⁰, I. Makarenko¹⁰, J. Malka¹⁰, S. Mergelmeyer³, F. Mohamad Idris^{6,c},
N. Mohammad Nasir⁶, V. Myronenko^{10,j}, K. Nagano¹⁴, T. Nobe²⁷, D. Notz¹⁰, R.J. Nowak³¹,
Yu. Onishchuk¹⁷, E. Paul³, W. Perlański^{31,y}, N.S. Pokrovskiy¹⁵, M. Przybycień⁸, P. Roloff^{10,k},
I. Rubinsky¹⁰, M. Ruspa²⁹, D.H. Saxon¹², M. Schioppa⁵, W.B. Schmidke^{21,t},
U. Schneekloth¹⁰, T. Schörner-Sadenius¹⁰, L.M. Shcheglova²⁰, R. Shevchenko^{17,q},
O. Shkola^{17,s}, Yu. Shyrma¹⁶, I. Singh^{4,b}, I.O. Skillicorn¹², W. Słomiński^{9,e}, A. Solano²⁸,
L. Stanco²³, N. Stefaniuk¹⁰, A. Stern²⁶, P. Stopa⁷, J. Sztuk-Dambietz^{13,g}, D. Szuba¹³,
J. Szuba¹⁰, E. Tassi⁵, K. Tokushuku^{14,n}, J. Tomaszewska^{31,z}, A. Trofymov^{17,r}, T. Tsurugai¹⁹,
M. Turcato^{13,g}, O. Turkot^{10,j}, T. Tymieniecka³², A. Verbytskyi²¹, O. Viazlo¹⁷, R. Walczak²²,
W.A.T. Wan Abdullah⁶, K. Wichmann^{10,j}, M. Wing^{30,w}, G. Wolf¹⁰, S. Yamada¹⁴,
Y. Yamazaki^{14,o}, N. Zakharchuk^{17,r}, A.F. Żarnecki³¹, L. Zawiejski⁷, O. Zenaiev¹⁰,
B.O. Zhautykov¹⁵, N. Zhmak^{16,p}, D.S. Zotkin²⁰

- 1 *INFN Bologna, Bologna, Italy*^A
- 2 *University and INFN Bologna, Bologna, Italy*^A
- 3 *Physikalisches Institut der Universität Bonn, Bonn, Germany*^B
- 4 *Panjab University, Department of Physics, Chandigarh, India*
- 5 *Calabria University, Physics Department and INFN, Cosenza, Italy*^A
- 6 *National Centre for Particle Physics, Universiti Malaya, 50603 Kuala Lumpur, Malaysia*^C
- 7 *The Henryk Niewodniczanski Institute of Nuclear Physics, Polish Academy of Sciences, Krakow, Poland*^D
- 8 *AGH-University of Science and Technology, Faculty of Physics and Applied Computer Science, Krakow, Poland*^D
- 9 *Department of Physics, Jagellonian University, Krakow, Poland*
- 10 *Deutsches Elektronen-Synchrotron DESY, Hamburg, Germany*
- 11 *Deutsches Elektronen-Synchrotron DESY, Zeuthen, Germany*
- 12 *School of Physics and Astronomy, University of Glasgow, Glasgow, United Kingdom*^E
- 13 *Hamburg University, Institute of Experimental Physics, Hamburg, Germany*^F
- 14 *Institute of Particle and Nuclear Studies, KEK, Tsukuba, Japan*^G
- 15 *Institute of Physics and Technology of Ministry of Education and Science of Kazakhstan, Almaty, Kazakhstan*
- 16 *Institute for Nuclear Research, National Academy of Sciences, Kyiv, Ukraine*
- 17 *Department of Nuclear Physics, National Taras Shevchenko University of Kyiv, Kyiv, Ukraine*
- 18 *Department of Physics, McGill University, Montréal, Québec, Canada H3A 2T8*^H
- 19 *Meiji Gakuin University, Faculty of General Education, Yokohama, Japan*^G
- 20 *Lomonosov Moscow State University, Skobeltsyn Institute of Nuclear Physics, Moscow, Russia*^I
- 21 *Max-Planck-Institut für Physik, München, Germany*
- 22 *Department of Physics, University of Oxford, Oxford, United Kingdom*^E
- 23 *INFN Padova, Padova, Italy*^A
- 24 *Dipartimento di Fisica e Astronomia dell' Università and INFN, Padova, Italy*^A
- 25 *Polytechnic University, Tokyo, Japan*^G
- 26 *Raymond and Beverly Sackler Faculty of Exact Sciences, School of Physics, Tel Aviv University, Tel Aviv, Israel*^J
- 27 *Department of Physics, Tokyo Institute of Technology, Tokyo, Japan*^G
- 28 *Università di Torino and INFN, Torino, Italy*^A
- 29 *Università del Piemonte Orientale, Novara, and INFN, Torino, Italy*^A

³⁰ *Physics and Astronomy Department, University College London, London, United Kingdom*^E

³¹ *Faculty of Physics, University of Warsaw, Warsaw, Poland*

³² *National Centre for Nuclear Research, Warsaw, Poland*

³³ *Department of Particle Physics and Astrophysics, Weizmann Institute, Rehovot, Israel*

³⁴ *Department of Physics, York University, Ontario, Canada M3J 1P3*^H

^A supported by the Italian National Institute for Nuclear Physics (INFN)

^B supported by the German Federal Ministry for Education and Research (BMBF), under contract No. 05 H09PDF

^C supported by HIR grant UM.C/625/1/HIR/149 and UMRG grants RU006-2013, RP012A-13AFR and RP012B-13AFR from Universiti Malaya, and ERGS grant ER004-2012A from the Ministry of Education, Malaysia

^D supported by the National Science Centre under contract No. DEC-2012/06/M/ST2/00428

^E supported by the Science and Technology Facilities Council, UK

^F supported by the German Federal Ministry for Education and Research (BMBF), under contract No. 05h09GUF, and the SFB 676 of the Deutsche Forschungsgemeinschaft (DFG)

^G supported by the Japanese Ministry of Education, Culture, Sports, Science and Technology (MEXT) and its grants for Scientific Research

^H supported by the Natural Sciences and Engineering Research Council of Canada (NSERC)

^I supported by RF Presidential grant N 3042.2014.2 for the Leading Scientific Schools and by the Russian Ministry of Education and Science through its grant for Scientific Research on High Energy Physics

^J supported by the Israel Science Foundation

- a* also funded by Max Planck Institute for Physics, Munich, Germany, now at Sant Longowal Institute of Engineering and Technology, Longowal, Punjab, India
- b* also funded by Max Planck Institute for Physics, Munich, Germany, now at Sri Guru Granth Sahib World University, Fatehgarh Sahib, India
- c* also at Agensi Nuklear Malaysia, 43000 Kajang, Bangi, Malaysia
- d* now at School of Physics and Astronomy, University of Birmingham, UK
- e* partially supported by the Polish National Science Centre projects DEC-2011/01/B/ST2/03643 and DEC-2011/03/B/ST2/00220
- f* now at Rockefeller University, New York, NY 10065, USA
- g* now at European X-ray Free-Electron Laser facility GmbH, Hamburg, Germany
- h* now at University of Liverpool, United Kingdom
- i* now at Physikalisches Institut, Universität Heidelberg, Germany
- j* supported by the Alexander von Humboldt Foundation
- k* now at CERN, Geneva, Switzerland
- l* Alexander von Humboldt Professor; also at DESY and University of Oxford
- m* also at DESY
- n* also at University of Tokyo, Japan
- o* now at Kobe University, Japan
- p* supported by DESY, Germany
- q* member of National Technical University of Ukraine, Kyiv Polytechnic Institute, Kyiv, Ukraine
- r* now at DESY ATLAS group
- s* member of National University of Kyiv - Mohyla Academy, Kyiv, Ukraine
- t* now at BNL, USA
- u* now at LNF, Frascati, Italy
- v* also at Max Planck Institute for Physics, Munich, Germany, External Scientific Member
- w* also at Universität Hamburg and supported by DESY and the Alexander von Humboldt Foundation
- x* also at Łódź University, Poland
- y* member of Łódź University, Poland
- z* now at Polish Air Force Academy in Deblin

1 Introduction

Exclusive electroproduction of vector mesons in deep inelastic scattering (DIS) at high energies is usually described as a multi-step process, as illustrated in Fig. 1: the electron emits a virtual photon, γ^* , with virtuality, Q^2 ; the γ^* fluctuates in leading-order QCD into a $q\bar{q}$ pair with a lifetime which, at large values of the γ^*p centre-of-mass energy, W , is long compared to the interaction time; and the $q\bar{q}$ pair interacts with the proton with momentum transfer squared, t , via a colour-neutral exchange, e.g. through a two-gluon ladder, and then hadronises into the vector meson, V .

In this paper, a measurement of the ratio of the cross sections of the reactions $\gamma^*p \rightarrow \psi(2S) + Y$ and $\gamma^*p \rightarrow J/\psi(1S) + Y$, where Y denotes either a proton or a low-mass proton-dissociative system, is presented. The $\psi(2S)$ and the $J/\psi(1S)$ have the same quark content, different radial distributions of the wave functions, and their mass difference is small compared to the HERA centre-of-mass energy. Therefore, this measurement allows QCD predictions of the wave function dependence of the $c\bar{c}$ -proton cross section to be tested. A suppression of the $\psi(2S)$ cross section relative to the $J/\psi(1S)$ is expected, as the $\psi(2S)$ wave function has a radial node close to the typical transverse separation of the virtual $c\bar{c}$ pair, as will be discussed in more detail in Section 7.1.

At HERA, deep inelastic exclusive $J/\psi(1S)$ electroproduction has been measured for $2 < Q^2 < 100 \text{ GeV}^2$, $30 < W < 220 \text{ GeV}$ and $|t| < 1 \text{ GeV}^2$ by the ZEUS collaboration [1] and for $2 < Q^2 < 80 \text{ GeV}^2$, $25 < W < 180 \text{ GeV}$ and $|t| < 1.6 \text{ GeV}^2$ by the H1 collaboration [2]. The H1 collaboration has also measured the quasi-elastic component, $\gamma^*p \rightarrow \psi(2S) + Y$, in DIS [2] and photoproduction [3], as well as the ratio of the $\psi(2S)$ to $J/\psi(1S)$ production cross sections.

The luminosity used for the measurement of $\sigma(ep \rightarrow e\psi(2S)Y)/\sigma(ep \rightarrow eJ/\psi(1S)Y)$ presented in this paper is 468 pb^{-1} and the kinematic range is $5 < Q^2 < 80 \text{ GeV}^2$, $30 < W < 210 \text{ GeV}$ and $|t| < 1 \text{ GeV}^2$. A sub-sample of 114 pb^{-1} of HERA I data was used for an additional measurement in the range $2 < Q^2 < 5 \text{ GeV}^2$. Events were selected with no activity in the central ZEUS detector in addition to signals from the scattered electron and the decay products of the $\psi(2S)$ or $J/\psi(1S)$. The decay channels used were $J/\psi(1S) \rightarrow \mu^+\mu^-$, $\psi(2S) \rightarrow \mu^+\mu^-$ and $\psi(2S) \rightarrow J/\psi(1S)\pi^+\pi^-$ with the subsequent decay $J/\psi(1S) \rightarrow \mu^+\mu^-$.

2 Experimental set-up

The measurement is based on data collected with the ZEUS detector at the HERA collider during the period 1996–2007 where an electron¹ beam of energy 27.5 GeV collided with a proton beam of either 820 GeV (1996–97) or 920 GeV (1998–2007). The integrated luminosity was 38 pb⁻¹ and 430 pb⁻¹ for ep centre-of-mass energies of 300 GeV and 318 GeV, respectively. The luminosity-weighted ep centre-of-mass energy is 317 GeV.

A detailed description of the ZEUS detector can be found elsewhere [4]. A brief outline of the components that are most relevant for this analysis is given below.

In the kinematic range of the analysis, charged particles were tracked in the central tracking detector (CTD) [5–7], which operated in a magnetic field of 1.43 T provided by a thin superconducting solenoid. The CTD consisted of 72 cylindrical drift-chamber layers, organised in nine superlayers covering the polar-angle² region $15^\circ < \theta < 164^\circ$. The transverse-momentum resolution for full-length tracks was $\sigma(p_T)/p_T = 0.0058p_T \oplus 0.0065 \oplus 0.0014/p_T$, with p_T in GeV. For the HERA II period, the CTD was complemented by a silicon microvertex detector (MVD) [8], which consisted of three cylindrical layers of silicon microstrip sensors in the central region and four planar disks in the forward region.

The high-resolution uranium–scintillator calorimeter (CAL) [9–12] consisted of three parts: the forward (FCAL), the barrel (BCAL) and the rear (RCAL) calorimeters. Each part was subdivided transversely into towers and longitudinally into one electromagnetic section (EMC) and either one (in RCAL) or two (in BCAL and FCAL) hadronic sections (HAC). The CAL energy resolutions, as measured under test-beam conditions, were $\sigma(E)/E = 0.18/\sqrt{E}$ for electrons and $\sigma(E)/E = 0.35/\sqrt{E}$ for hadrons, with E in GeV.

The muon system consisted of rear, barrel (R/BMUON) and forward (FMUON) tracking detectors. The R/BMUON consisted of limited-streamer (LS) tube chambers placed behind the RCAL (BCAL), inside and outside a magnetised iron yoke surrounding the CAL. The barrel and rear muon chambers covered polar angles from 34° to 135° and from 135° to 171° , respectively. The FMUON consisted of six trigger planes of LS tubes and four planes of drift chambers covering the angular region from 5° to 32° . The muon system exploited the magnetic field of the iron yoke and, in the forward direction, of two iron toroids magnetised to ≈ 1.6 T to provide an independent measurement of the muon momenta.

The iron yoke surrounding the CAL was instrumented with proportional drift chambers to form the backing calorimeter (BAC) [13]. The BAC consisted of 5142 aluminium

¹ Hereafter electron refers to both electrons and positrons unless otherwise stated.

² The ZEUS coordinate system is a right-handed Cartesian system, with the Z axis pointing in the proton beam direction, referred to as the “forward direction”, and the X axis pointing towards the centre of HERA. The coordinate origin is at the nominal beam-crossing point [4].

chambers inserted into the gaps between 7.3 cm thick iron plates (10, 9 and 7 layers in the forward, barrel and rear directions, respectively). The chambers were typically 5 m long and had a wire spacing of 1.5 cm. The anode wires were covered by 50 cm long cathode pads. The BAC was equipped with energy readout and position-sensitive readout for muon tracking. The former was based on 1692 pad towers ($50 \times 50 \text{ cm}^2$), providing an energy resolution of $\sigma(E)/E \approx 100\%/\sqrt{E}$, with E in GeV. The position information from the wires allowed the reconstruction of muon trajectories in two dimensions (XY in the barrel and YZ in the endcaps) with a spatial accuracy of a few mm.

The luminosity was measured using the Bethe–Heitler reaction $ep \rightarrow e\gamma p$ by a luminosity detector which consisted of a lead–scintillator calorimeter [14–16] and, additionally in HERA II, a magnetic spectrometer [17].

3 Monte Carlo simulations

The DIFFVM [18] Monte Carlo (MC) programme was used for simulating exclusive vector meson production, $ep \rightarrow eVp$, where V denotes the produced vector meson with mass M_V . For the event generation, the following cross-section parameterisations were used: $(1 + Q^2/M_V^2)^{-1.5}$ for transverse virtual photons; $(Q/M_V)^2$ for the cross-section ratio of longitudinal to transverse photons; $\exp(-b|t|)$, with $b = 4 \text{ GeV}^{-2}$ for the dependence on t ; s -channel helicity conservation for the production of $V \rightarrow \mu^+\mu^-$; and a flat angular distribution for the $\psi(2S) \rightarrow J/\psi(1S)\pi^+\pi^-$ decay. As described in Section 4.3, the simulated events, after taking into account the acceptance, are reweighted to match the measured distributions. Proton-dissociative $\psi(2S)$ and $J/\psi(1S)$ events were not simulated. In the analysis of the experimental data, events were selected with proton-dissociative masses $M_Y \lesssim 4 \text{ GeV}$, for which the Q^2 and W distributions of $\psi(2S)$ and $J/\psi(1S)$ events are expected to be similar. The fact that proton-dissociative events favour larger $|t|$ values is taken into account by the reweighting procedure, where it has been assumed that the relative contribution is the same for $\psi(2S)$ and $J/\psi(1S)$ production.

Radiative effects were not simulated. The largest contribution is expected to come from the initial-state radiation of the electrons, however, as the $\psi(2S) - J/\psi(1S)$ mass difference is small compared to W , the kinematics of both reactions are similar and radiative effects are expected to cancel in the cross-section ratio.

Non-resonant electroweak dimuon production (Bethe–Heitler background) was simulated using the dimuon programme GRAPE [19]. The event sample contains both exclusive and proton-dissociative events with a mass of the dissociated proton system, $M_Y < 25 \text{ GeV}$.

The generated MC events were passed through the ZEUS detector and trigger simulation programmes based on GEANT 3 [20]. They were then reconstructed and analysed with the same programmes as used for the data.

4 Event selection and signal extraction

4.1 Event selection

A three-level trigger system [4, 21, 22] was used to select events online. For this analysis, DIS events were selected with triggers containing a candidate scattered electron. Further triggers were used with a less stringent electron-candidate selection in coincidence with a muon candidate or with two tracks.

The offline event selection required an electron candidate in the RCAL with an energy $E'_e > 10$ GeV as reconstructed using an algorithm based on a neural network [23]. The position of the scattered electron was required to be outside areas with significant inactive material in front of the calorimeter.

To select events containing exclusively produced $J/\psi(1S)$ and $\psi(2S)$ vector mesons, the following additional requirements were imposed:

- the Z coordinate of the interaction vertex reconstructed from the tracks was required to be within ± 30 cm of the nominal interaction point;
- in addition to the scattered electron, two oppositely charged muons were required. Muons were identified using the GMUON algorithm [24] with muon quality ≥ 1 . This algorithm required a track with momentum above 1 GeV to be matched with a cluster in the CAL. The cluster was required to be consistent with a muon using an algorithm based on a neural network [25];
- for selecting $J/\psi(1S) \rightarrow \mu^+\mu^-$ and $\psi(2S) \rightarrow \mu^+\mu^-$ events, no additional tracks were allowed;
- for selecting $\psi(2S) \rightarrow J/\psi(1S)\pi^+\pi^-$ events, exactly two oppositely charged tracks were required in addition to the two muons. The tracks had to cross at least three CTD superlayers, produce hits in the first CTD superlayer or in the MVD and the transverse momentum of each track had to exceed 0.12 GeV;
- events with calorimeter clusters with energies above 0.4 GeV, not associated with the electron or the decay products of the vector meson, were rejected. The threshold value of this cut was optimised by minimising event loss from calorimeter noise fluctuations and maximising the rejection of non-exclusive vector-meson production with additional energy deposits in the CAL.

The last three requirements significantly reduced the background from non-exclusive charmonium production and also removed proton-dissociative events with diffractive masses $M_Y \gtrsim 4$ GeV [19].

4.2 Reconstruction of the kinematic variables and signal extraction

The kinematic variables, Q^2 , W and t were used in the analysis. The constrained method [26] was used to reconstruct Q^2 according to

$$Q^2 = 2E_e E'_e (1 + \cos \theta_e),$$

where

$$E'_e = \frac{2E_e - (E - p_Z)_V}{1 - \cos \theta_e}.$$

Here E_e denotes the electron beam energy and E'_e and θ_e the energy and the polar angle of the scattered electron, respectively. The quantity $(E - p_Z)_V$ denotes the difference of the energy and the Z component of the momentum of V . The momentum components of the vector-meson candidate, V , and its effective mass, M_V , were obtained from the momentum vectors of the decay products measured by the tracking detectors. The values of W and t were calculated using

$$W = \sqrt{2 E_p (E - p_Z)_V - Q^2 + M_p^2}$$

and

$$-t = (\vec{p}'_{T,e} + \vec{p}_{T,V})^2.$$

Here E_p is the proton beam energy, M_p is the proton mass and $\vec{p}'_{T,e}$ and $\vec{p}_{T,V}$ are the transverse-momentum vectors of the scattered electron and of the vector-meson candidate, respectively. The kinematic range for the analysis of the HERA II (HERA I) data is $5 (2) < Q^2 < 80 \text{ GeV}^2$, $30 < W < 210 \text{ GeV}$ and $|t| < 1 \text{ GeV}^2$. The range of Bjorken x , $x_{\text{Bj}} \approx (M_V^2 + Q^2)/(W^2 + Q^2)$, probed by the measurements is $2 \times 10^{-4} < x_{\text{Bj}} < 10^{-2}$.

Figure 2 shows the $\mu^+\mu^-$ mass distribution for the selected events in the region $5 < Q^2 < 80 \text{ GeV}^2$. Clear $J/\psi(1S)$ and $\psi(2S)$ peaks are seen. No other significant peak is observed. The background was fit by a straight line in the side-bands of the signals: $2.0 < M_{\mu\mu} < 2.62 \text{ GeV}$ and $4.05 < M_{\mu\mu} < 5.0 \text{ GeV}$.

The ratio of $\psi(2S)$ to $J/\psi(1S)$ events for the $\mu^+\mu^-$ decay channel was obtained from the ratio of the number of events above background in the range $3.59 < M_{\mu\mu} < 3.79 \text{ GeV}$ to the corresponding number in the range $3.02 < M_{\mu\mu} < 3.17 \text{ GeV}$. According to a detailed MC study, this choice minimises the systematic uncertainty due to the uncertainties of the mass-resolution function and the shape of the background. The difference in widths of the mass bins chosen takes into account the worsening of the mass resolution with increasing $M_{\mu\mu}$.

To study the systematic uncertainty related to the background subtraction, a quadratic background function was used and the widths of the $M_{\mu\mu}$ intervals for the signal determination were varied. The Bethe–Heitler MC events provide a good description of

the background shape and its absolute normalisation after acceptance correction agrees with the measured rate within the estimated uncertainty of about 20%. Given this uncertainty, the linear fit described in the previous paragraph was used for the background subtraction.

Figure 3 shows a scatter plot of $\Delta M = M_{\mu\mu\pi\pi} - M_{\mu\mu}$ versus $M_{\mu\mu}$ and the ΔM and $M_{\mu\mu\pi\pi}$ distributions for $3.02 < M_{\mu\mu} < 3.17$ GeV. As expected, the ΔM distribution shows a narrow peak with a width of about 5 MeV at the nominal $\psi(2S) - J/\psi(1S)$ mass difference of 589.2 MeV. The mass ranges of $3.02 < M_{\mu\mu} < 3.17$ GeV and $0.5 < \Delta M < 0.7$ GeV were chosen to compute the ratio of $\psi(2S)$ to $J/\psi(1S)$ events. As can be seen from Fig. 3, there is hardly any background in the $\psi(2S)$ signal region; an upper limit of three events at 90% confidence level was estimated for the background.

The numbers of events and their statistical uncertainties used for the further analysis for the kinematic region $5 < Q^2 < 80$ GeV², $30 < W < 210$ GeV and $|t| < 1$ GeV² are 2224 ± 48 , 97 ± 10 and 80 ± 13 for the $J/\psi \rightarrow \mu^+\mu^-$, $\psi(2S) \rightarrow J/\psi(1S) \pi^+\pi^-$ and the $\psi(2S) \rightarrow \mu^+\mu^-$ decays, respectively. For $2 < Q^2 < 5$ GeV², the corresponding numbers are 297 ± 18 , 11.0 ± 3.3 and 4.4 ± 4.1 .

4.3 Comparison of measured and simulated distributions

In order to determine the acceptance using simulated events, simulated and measured distributions have to agree. To achieve this, the simulated events had to be reweighted. The reweighting functions for the $J/\psi(1S)$ as well as for the $\psi(2S)$ events were obtained by comparing the measured distributions of the $J/\psi(1S) \rightarrow \mu^+\mu^-$ sample to the simulated distributions. For the reweighting of the t and Q^2 distributions, a two-dimensional function was used. No reweighting was required for the W distribution. The following reweighting function was used for the angular distribution for the vector meson decays into $\mu^+\mu^-$:

$$f(\Phi_h) = 1 - \epsilon \cdot \cos(2\Phi_h) \cdot (2r_{11}^1 + r_{00}^1) + \sqrt{2\epsilon(1+\epsilon)} \cdot \cos(\Phi_h) \cdot (2r_{11}^5 + r_{00}^5).$$

The helicity angle Φ_h is the angle between the production and scattering planes, where the production plane is defined by the three-momenta of the photon and the vector meson, and the scattering plane is defined by the three-momenta of the incoming and the scattered electron. The elements of the spin-density matrix, r_{ij}^k , were obtained by fitting the weighted simulated events to the measured decay angular distribution of $J/\psi(1S)$. The dominant contribution comes from r_{00}^1 , compatible with s -channel helicity conservation. The quantity ϵ denotes the ratio of the longitudinal to the transverse virtual-photon flux, which was set to unity in the kinematic range of the measurement. In the MC simulation, the fitted angular distribution was used as reweighting function for both vector-meson decays into $\mu^+\mu^-$, whereas no reweighting was applied for the flatly simulated decay $\psi(2S) \rightarrow J/\psi(1S) \pi^+\pi^-$.

The measured $|t|$ distributions for $J/\psi(1S)$ and $\psi(2S)$ have been fitted separately by single exponentials, and by the sum of two exponentials. It is found that the second exponential is not significant, and that the slopes for $J/\psi(1S)$ and $\psi(2S)$ agree within the statistical uncertainties. This confirms the validity of the assumptions made in Section 3: given the limited statistics of the data sample, it is neither necessary to simulate proton dissociative events nor to weight the $|t|$ distributions of the $J/\psi(1S)$ and $\psi(2S)$ differently.

The comparisons of the Q^2 , W and $|t|$ distributions between data and reweighted MC events normalised to the number of measured events are shown in Figs. 4, 5 and 6 for the $J/\psi(1S) \rightarrow \mu^+\mu^-$, $\psi(2S) \rightarrow \mu^+\mu^-$ and $\psi(2S) \rightarrow J/\psi(1S) \pi^+\pi^-$ channels, respectively. Agreement is observed for all distributions.

5 Cross-section ratio $\psi(2S)$ to $J/\psi(1S)$

The following cross-section ratios, $\sigma_{\psi(2S)}/\sigma_{J/\psi(1S)}$, have been measured: $R_{\mu\mu}$ for $\psi(2S) \rightarrow \mu^+\mu^-$, $R_{J/\psi \pi\pi}$ for $\psi(2S) \rightarrow J/\psi(1S) \pi^+\pi^-$ and R_{comb} for the combination of the two decay modes. In each case the decay $J/\psi(1S) \rightarrow \mu^+\mu^-$ was used.

5.1 Determination of the cross-section ratio

The cross-section ratios were calculated using

$$R_{\mu\mu} = \left(\frac{N_{\mu\mu}^{\psi(2S)}}{B(\psi(2S) \rightarrow \mu^+\mu^-) \cdot A_{\mu\mu}^{\psi(2S)}} \right) / \left(\frac{N_{\mu\mu}^{J/\psi(1S)}}{B(J/\psi(1S) \rightarrow \mu^+\mu^-) \cdot A_{\mu\mu}^{J/\psi(1S)}} \right) \text{ and}$$

$$R_{J/\psi \pi\pi} = \left(\frac{N_{J/\psi \pi\pi}^{\psi(2S)}}{B(\psi(2S) \rightarrow J/\psi(1S) \pi^+\pi^-) \cdot A_{J/\psi \pi\pi}^{\psi(2S)}} \right) / \left(\frac{N_{\mu\mu}^{J/\psi(1S)}}{A_{\mu\mu}^{J/\psi(1S)}} \right),$$

where N_i^j denotes the number of observed signal events for the charmonium state j with the decay mode i , and A_i^j the corresponding acceptance determined from the ratio of reconstructed to generated MC events after reweighting. The following values were used for the branching fractions: $B(J/\psi(1S) \rightarrow \mu^+\mu^-) = (5.93 \pm 0.06)\%$, $B(\psi(2S) \rightarrow \mu^+\mu^-) = (0.77 \pm 0.08)\%$ and $B(\psi(2S) \rightarrow J/\psi(1S) \pi^+\pi^-) = (33.6 \pm 0.4)\%$ [27].

The combined cross-section ratio, R_{comb} , was obtained using the weighted average of the cross sections determined for the two $\psi(2S)$ decay modes. For the weights, the statistical uncertainties were used. The different R values were determined in the full kinematic region as well as in bins of Q^2 , W and $|t|$. The results are reported in Section 6.

5.2 Systematic uncertainties

The systematic uncertainties of the R values were obtained by performing for each source of uncertainty a suitable variation in order to determine the change of R relative to its nominal value. The following sources of systematic uncertainties were considered:

- reducing the $M_{\mu\mu}$ range for the $J/\psi(1S)$ from the nominal value 3.02 – 3.17 GeV to 3.05 – 3.15 GeV and for the $\psi(2S)$ from the nominal value 3.59 – 3.79 GeV to 3.62 – 3.75 GeV, changes the values of $R_{\mu\mu}$ by $\approx +2\%$ and of $R_{J/\psi\pi\pi}$ by $\approx +1.5\%$;
- increasing the $M_{\mu\mu}$ range for the $J/\psi(1S)$ from the nominal value 3.02 – 3.17 GeV to 2.97 – 3.22 GeV and for the $\psi(2S)$ from the nominal value 3.59 – 3.79 GeV to 3.55 – 3.80 GeV, changes the values of $R_{\mu\mu}$ by $\approx 6\%$ and of $R_{J/\psi\pi\pi}$ by $\approx -0.5\%$;
- changing the cut on the transverse momenta p_T of the pion tracks from the nominal value of 0.12 GeV to 0.15 GeV changes the values of $R_{J/\psi\pi\pi}$ by $\approx -4.5\%$;
- changing the background fit function from linear to quadratic changes the values of $R_{\mu\mu}$ by $\approx -11\%$ and of $R_{J/\psi\pi\pi}$ by $\approx +0.5\%$;
- changing the reconstruction from the constrained to the electron method [28] changes the values of $R_{\mu\mu}$ and of $R_{J/\psi\pi\pi}$ by $\approx +1.5\%$;
- not applying the reweighting of the simulated events discussed in Section 4.3 changes the values of $R_{\mu\mu}$ by $\approx -3\%$ and of $R_{J/\psi\pi\pi}$ by $\approx -1\%$;
- applying different cuts on the total number of tracks, including tracks not associated with the event vertex, changes $R_{\mu\mu}$ by $\approx -5\%$ and $R_{J/\psi\pi\pi}$ by $\approx +3\%$.

The total systematic uncertainty was obtained from the separate quadratic sums of the positive and negative changes. The estimated total systematic uncertainties are $\delta R_{\mu\mu} = {}^{+7}_{-14}\%$, $\delta R_{J/\psi\pi\pi} = {}^{+4}_{-5}\%$ and $\delta R_{\text{comb}} = {}^{+3}_{-5}\%$. For the calculation of δR_{comb} , the uncertainties of the two measurements were assumed to be uncorrelated.

6 Results

The results for the three cross-section ratios $\sigma_{\psi(2S)}/\sigma_{J/\psi(1S)}$: $R_{\mu\mu}$ for $\psi(2S) \rightarrow \mu^+\mu^-$, $R_{J/\psi\pi\pi}$ for $\psi(2S) \rightarrow J/\psi(1S)\pi^+\pi^-$ and R_{comb} for the combination, are reported in Table 1 for the kinematic range $5 < Q^2 < 80 \text{ GeV}^2$, $30 < W < 210 \text{ GeV}$ and $|t| < 1 \text{ GeV}^2$ for the total integrated luminosity of 468 pb^{-1} . The cross-section ratios, differential in Q^2 , W and $|t|$, together with the additional measurement between $2 < Q^2 < 5 \text{ GeV}^2$, corresponding to an integrated luminosity of 114 pb^{-1} , are shown in Table 2. The data contain a background of charmonium production with diffractive masses $M_Y \lesssim 4 \text{ GeV}$. Assuming that the $\psi(2S)$ to $J/\psi(1S)$ cross-section ratio for exclusive charmonium

production is the same as for charmonium production with low M_Y , the determination of the R values for exclusive production are not affected.

Figure 7 shows the values of R_{comb} as a function of Q^2 , W and $|t|$. The results for the W and $|t|$ dependence are shown for $5 < Q^2 < 80 \text{ GeV}^2$. The results for the Q^2 dependence also include the additional measurement for $2 < Q^2 < 5 \text{ GeV}^2$ from the HERA I data. As a function of W and $|t|$, the values of R_{comb} are compatible with a constant. For the Q^2 dependence, a positive slope is observed with the significance of ≈ 2.5 standard deviations.

As a cross check it was verified that the ratio $R_{J/\psi \pi\pi}$ to $R_{\mu\mu}$ is compatible with 1. For the entire kinematic range of the measurement a value of $R_{\psi(2S)} = R_{J/\psi \pi\pi}/R_{\mu\mu} = 1.1 \pm 0.2 \text{ }^{+0.2}_{-0.1} \pm 0.1$ is found. The first error is the statistical uncertainty, the second the systematic uncertainty of the measurement and the third the uncertainty of the $\psi(2S)$ branching fractions. The ratio is consistent with unity for the entire kinematic region and also as a function of the kinematic variables, Q^2 , W and $|t|$, as shown in Tables 1 and 2.

In Fig. 8, the results are also compared to the previous H1 measurements [2]. The results are compatible. The H1 collaboration has also measured $R = \sigma_{\psi(2S)}/\sigma_{J/\psi(1S)}$ in photoproduction ($Q^2 \approx 0$), and found a value of $R = 0.150 \pm 0.035$ [3], which is consistent with the trend of the Q^2 dependence presented in this paper. The comparison of the results to various model predictions is presented in the Section 7.

7 Comparison to model predictions

In this section, the cross-section ratio $R = \sigma_{\psi(2S)}/\sigma_{J/\psi(1S)}$ in DIS, presented in this paper, and the results from the H1 collaboration in DIS [2] and photoproduction [3], are compared to model predictions from six different groups labelled by the names of the authors: HIKT, KNNPZZ, AR, LP, FFJS and KMW.

7.1 Individual models

In order to calculate the exclusive production of vector charmonium states according to the diagram shown in Fig. 1, the following components need to be determined:

- the probability of finding a $c\bar{c}$ -dipole of transverse size r and impact parameter b in the photon in the infinite momentum frame;
- the $c\bar{c}$ -dipole scattering amplitude or cross section of the proton as a function of r , b and $x_{Bj} \approx (M_V + Q^2)/(W^2 + Q^2)$;

- the probability that the $c\bar{c}$ -dipole forms the vector charmonium state V in the infinite momentum frame.

The probability distribution of $c\bar{c}$ -dipoles in the photon can be calculated in QED [29,30]. For the probability that the $c\bar{c}$ -dipole forms the vector charmonium state, its centre-of-mass wave function has to be boosted into the infinite momentum frame, which is done using the boosted Gaussian model [31]. For the evaluation of the $c\bar{c}$ -dipole scattering amplitude, different QCD calculations are used. All models discussed predict a Q^2 dependent suppression of exclusive $\psi(2S)$ relative to $J/\psi(1S)$ production. For the models, which explicitly use the wave functions of the vector mesons, this is caused by the node of the radial $\psi(2S)$ wave function, which leads to a destructive interference of the contributions to the production amplitude from small and large dipoles.

Hüfner et al. [32] (HIKT) use two phenomenological parameterisations of the $c\bar{c}$ -dipole cross section, GBW [33] and KST [34], which both describe the low- x inclusive DIS data from HERA. For the centre-of-mass wave functions of the $J/\psi(1S)$ and $\psi(2S)$, they use four different phenomenological potentials, BT, LOG, COR and POW, and c -quark masses between 1.48 and 1.84 GeV. However, only the models with c -quark masses around 1.5 GeV, GBW–BT and GBW–LOG, are able to describe the cross sections of exclusive $J/\psi(1S)$ production measured at HERA. For the boost of the charmonium wave functions into the infinite momentum frame, they find the wave function from the Schrödinger equation and then boost the result. A major progress made [32] is the inclusion of the Melosh spin rotation into the boosting procedure, which enhances the $\psi(2S)$ to $J/\psi(1S)$ cross-section ratio by a factor of two to three.

The model of Kopeliovich et al. [35–38] (KNNPZZ) uses the running gBFKL approach for the $c\bar{c}$ -dipole cross section and the diffractive slope for its t dependence. The parameterisation of the $c\bar{c}$ -dipole cross section used gives a quantitative description of the rise of the proton structure function at small x values as well as of the Q^2 and W dependence of diffractive $J/\psi(1S)$ production. KNNPZZ use parameterisations of the vector meson wave functions, inspired by the conventional spectroscopic models and short-distance behaviour driven by hard QCD gluon exchange. For the $\psi(2S)$, an additional parameter is introduced, which controls the position of the node.

Armesto and Rezaeian [39] (AR) calculate the $c\bar{c}$ -dipole cross section using the Impact-Parameter-dependent Color Glass Condensate model (b-CGC) [40] as well as the Saturation (IP-Sat) [41] dipole model, recently updated with fits to the HERA combined data [42, 43]. In the b-CGC model, which is restricted to the gluon sector, saturation is driven by the BFKL evolution, and its validity is therefore limited to $x_{Bj} \lesssim 10^{-2}$. The IP-Sat model uses DGLAP evolution and smoothly matches the perturbative QCD limit at high values of Q^2 . For the calculation of the light-cone $J/\psi(1S)$ and $\psi(2S)$ wave functions, the boosted Gaussian model and the leptonic decay widths $\Gamma_{ee}^{J/\psi(1S)}$ and $\Gamma_{ee}^{\psi(2S)}$ are used.

Lappi and Mäntysaari [44, 45] (LM) use the BFKL evolution as well as the IP-Sat model to predict vector-meson production in ep and electron–ion collisions in the dipole picture. The wave functions of the $J/\psi(1S)$ and $\psi(2S)$ have been calculated according to the procedure developed previously [46, 47] and the low- x inclusive HERA data have been used to constrain the $c\bar{c}$ -dipole cross section.

Fazio et al. [48] (FFJS) use a two-component Pomeron model to predict the cross sections for vector-meson production. A normalisation factor of $f_{\psi(2S)}^{-1} = 0.45$ ensures that the value of the $\psi(2S)$ cross section is the same as for the other vector mesons at the same values of W , t and $Q_V^2 = M_V^2 + Q^2$ (i.e. $f_{\psi(2S)} \sigma_{\psi(2S)} = \sigma_{J/\psi}$). In this model the Q^2 dependence of the $\psi(2S)$ to $J/\psi(1S)$ suppression is caused by the difference of Q_V^2 at a fixed Q^2 due to the $\psi(2S) - J/\psi(1S)$ mass difference.

Kowalski, Motyka and Watt [46] (KMW) assume the universality of the production of vector quarkonia states in the scaling variable Q_V^2 in their calculation of R . With the assumptions that the $c\bar{c} \rightarrow V$ transition is proportional to the leptonic decay width Γ_{ee}^V and that the interaction is mediated by two-gluon exchange and therefore proportional to $(\alpha_s(Q_V) x_{Bj} g(x_{Bj}, Q_V^2))^2$, R is given in the leading-logarithmic approximation [49–51] by

$$R = \left(\frac{\alpha_s(Q_{\psi(2S)})}{\alpha_s(Q_{J/\psi(1S)})} \right)^2 \frac{\Gamma_{\psi(2S)} M_{\psi(2S)}^{1-\delta}}{\Gamma_{J/\psi(1S)} M_{J/\psi(1S)}^{1-\delta}} \left(\frac{Q_{\psi(2S)}}{Q_{J/\psi(1S)}} \right)^{-6-4\bar{\lambda}+\delta}. \quad (1)$$

The running strong coupling constant, $\alpha_s(Q)$, and the gluon density, $g(x, Q^2)$, are evaluated at Q_V and x_{Bj} . For small x_{Bj} values, the gluon density can be parameterised as $x_{Bj} g(x_{Bj}, Q_V^2) \propto x_{Bj}^{-\lambda(Q_V)}$ with $\lambda(Q_V) \simeq \bar{\lambda} = 0.25$ in the Q_V region of this measurement. The parameter δ depends on the choice of the charmonium wave functions. For the non-relativistic wave functions $\delta = 0$ [49–51] and for the relativistic boosted Gaussian model $\delta \approx 2$ [46]. Note that the Q^2 dependence of the ratio R in this approach is driven by kinematic factors and not by the shapes and nodes of the charmonia wave functions.

7.2 Comparison of models and data

In the kinematic region of the measurement, all models predict only a weak W and $|t|$ dependence of R , consistent with the data, as shown in Fig. 7. Therefore, only the comparison of the model calculations with the measurements as a function of Q^2 is presented in Fig. 8. It can be seen that all models predict an increase of R with Q^2 , which is also observed experimentally. In the following discussion, the models are discussed in the sequence from higher to lower predicted R values at high Q^2 .

From the HIKT calculations, the results for R for the two charmonium potentials BT and LOG with c -quark mass around 1.5 GeV and the GBW model for the $c\bar{c}$ -dipole cross section are shown. The difference of the results when using the KST dipole cross sections are small. For Q^2 values below 24 GeV², the predicted R values for the BT model are

significantly larger than the measured values, whereas the values predicted by the LOG model agree with the data.

For the AR calculations, the results for the b-CGC and IP-Sat models of the dipole cross sections are shown in the figure. For Q^2 values below 24 GeV^2 , the b-CGC prediction for R is significantly higher than the data, whereas the IP-Sat model gives a good description of the data for the entire Q^2 range.

The KMW model with $\delta = 0$ provides a good description of the observed Q^2 dependence of R , whereas the prediction for $\delta = 2$ is about 2 standard deviations below the R value measured for $Q^2 > 24 \text{ GeV}^2$.

The predictions of the models FFJS, KNNPZZ and LM, in spite of differences in the values of R at low Q^2 values, also provide fair descriptions of the measurements.

Some discrimination of the different models is possible, although a large spread in the predictions indicates that the uncertainty on the theory is large.

8 Summary

The cross-section ratio $R = \sigma_{\psi(2S)}/\sigma_{J/\psi(1S)}$ in exclusive electroproduction was measured with the ZEUS experiment at HERA in the kinematic range $2 < Q^2 < 80 \text{ GeV}^2$, $30 < W < 210 \text{ GeV}$ and $|t| < 1 \text{ GeV}^2$, with an integrated luminosity of 468 pb^{-1} . The decay channels used were $\mu^+\mu^-$ and $J/\psi(1S) \pi^+\pi^-$ for the $\psi(2S)$ and $\mu^+\mu^-$ for the $J/\psi(1S)$. The cross-section ratio has been determined as a function of Q^2 , W and $|t|$. The results are consistent with a constant value of R as a function of W and t , but show a tendency to increase with increasing Q^2 . A number of model calculations are compared to the measured Q^2 dependence of R .

Acknowledgements

We appreciate the contributions to the construction, maintenance and operation of the ZEUS detector of many people who are not listed as authors. The HERA machine group and the DESY computing staff are especially acknowledged for their success in providing excellent operation of the collider and the data-analysis environment. We thank the DESY directorate for their strong support and encouragement. We also thank Y. Ivanov, L. Jenkovski, B. Kopeliovich, L. Motyka, A. Rezaeian and A. Sali for interesting discussions and for providing the results of their calculations.

References

- [1] ZEUS Coll., S. Chekanov et al., Nucl. Phys. **B 695**, 3 (2004).
- [2] H1 Coll., C. Adloff et al., Eur. Phys. J. **C 10**, 373 (1999).
- [3] H1 Coll., C. Adloff et al., Phys. Lett. **B 421**, 385 (1998).
- [4] ZEUS Coll., U. Holm (ed.), The ZEUS Detector. Status Report (unpublished), DESY (1993). <http://www-zeus.desy.de/bluebook/bluebook.html>.
- [5] N. Harnew et al., Nucl. Inst. Meth. **A 279**, 290 (1989).
- [6] B. Foster et al., Nucl. Phys. Proc. Suppl. **B 32**, 181 (1993).
- [7] B. Foster et al., Nucl. Inst. Meth. **A 338**, 254 (1994).
- [8] A. Polini et al., Nucl. Inst. Meth. **A 581**, 656 (2007).
- [9] M. Derrick et al., Nucl. Inst. Meth. **A 309**, 77 (1991).
- [10] A. Andresen et al., Nucl. Inst. Meth. **A 309**, 101 (1991).
- [11] A. Caldwell et al., Nucl. Inst. Meth. **A 321**, 356 (1992).
- [12] A. Bernstein et al., Nucl. Inst. Meth. **A 336**, 23 (1993).
- [13] I. Kudla et al., Nucl. Inst. Meth. **A 300**, 480 (1991).
- [14] J. Andruszków et al., Preprint DESY-92-066, DESY (1992).
- [15] ZEUS Coll., M. Derrick et al., Z. Phys. **C 63**, 391 (1994).
- [16] J. Andruszków et al., Acta Phys. Polon. **B 32**, 2025 (2001).
- [17] M. Helbich et al., Nucl. Inst. Meth. **A 565**, 572 (2006).
- [18] B. List and A. Mastroberardino, *Proc. Workshop on Monte Carlo Generators for HERA Physics*, A.T. Doyle, G. Grindhammer, G. Ingelman, H. Jung (eds.), p. 396, DESY, Hamburg, Germany (1999). Also in preprint DESY-PROC-1999-02.
- [19] T. Abe, Comp. Phys. Comm. **136**, 126 (2001).
- [20] R. Brun et al., GEANT3, Technical Report CERN-DD/EE/84-1, CERN, 1987.
- [21] P.D. Allfrey et al., Nucl. Inst. Meth. **A 580**, 1257 (2007).
- [22] W.H. Smith, K. Tokushuku and L.W. Wiggers, *Proc. Computing in High-Energy Physics (CHEP), Annecy, France, Sept. 1992*, C. Verkerk and W. Wojcik (eds.), p. 222. CERN, Geneva, Switzerland (1992). Also in preprint DESY-92-150B.
- [23] H. Abramowicz, A. Caldwell and R. Sinkus, Nucl. Inst. Meth. **A 365**, 508 (1995).

- [24] I. Bloch, Ph.D. Thesis, Hamburg University, Report DESY-THESIS-2005-034 (2005).
- [25] V.A. Kuzmin, Nucl. Inst. Meth. **A 453**, 336 (2000).
- [26] ZEUS Coll., J. Breitweg et al., Eur. Phys. J. **C 6**, 603 (1999).
- [27] J. Beringer et al., Phys. Rev. **D 86**, 010001 (2012).
- [28] K.C. Höger, *Proc. Workshop on Physics at HERA*, W. Buchmüller and G. Ingelman (eds.), Vol. 1, p.43, DESY, Hamburg, Germany (1992).
- [29] J.B. Kogut and D.E. Soper, Phys. Rev. **D 1**, 2901 (1970).
- [30] J.D. Bjorken, J.B. Kogut and D.E. Soper, Phys. Rev. **D 3**, 1382 (1971).
- [31] M.V. Terentev, Sov. J. Nucl. Phys. **24**, 106 (1976).
- [32] J. Hüfner et al., Phys. Rev. **D 62**, 094022 (2000).
- [33] K.J. Golec-Biernat and M. Wüsthoff, Phys. Rev. **D 59**, 014017 (1998).
- [34] B.Z. Kopeliovich, A. Schäfer and A.V. Tarasov, Phys. Rev. **D 62**, 054022 (2000).
- [35] B.Z. Kopeliovich and B.G. Zakharov, Phys. Rev. **D 44**, 3466 (1991).
- [36] B.Z. Kopeliovich, Phys. Lett. **B 324**, 469 (1994).
- [37] J. Nemchik, N.N. Nikolaev and B.G. Zakharov, Phys. Lett. **B 341**, 228 (1994).
- [38] J. Nemchik et al., J. Exp. Theor. Phys. **86**, 1054 (1998).
- [39] N. Armesto and A.H. Reazeian, Phys. Rev. **D 90**, 054003 (2014).
- [40] A.H. Reazeian and I. Schmidt, Phys. Rev. **D 88**, 074016 (2013).
- [41] A.H. Reazeian et al., Phys. Rev. **D 87**, 034002 (2014).
- [42] H1 Coll., F.D. Aaron et al., JHEP **01**, 109 (2010).
- [43] H1 and ZEUS Coll., H. Abramowicz et al., Eur. Phys. J. **C 73**, 2311 (2013).
- [44] T. Lappi and H. Mäntysaari, Phys. Rev. **C 83**, 065202 (2011).
- [45] T. Lappi and H. Mäntysaari, PoS (DIS2014), 069 (2014).
- [46] H. Kowalski, L. Motyka and G. Watt, Phys. Rev. **D 74**, 074016 (2006).
- [47] B. Cox, J. Forshaw and R. Sandapen, JHEP **0906**, 034 (2009).
- [48] S. Fazio et al., Phys. Rev. **D 90**, 016007 (2014).
- [49] M.G. Ryskin, Z. Phys. **C 57**, 89 (1993).
- [50] S.J. Brodsky et al., Phys. Rev. **D 50**, 3134 (1994).

[51] S.P. Jones et al., JHEP **1311**, 085 (2013).

[52] G.D. Lafferty and T.R. Wyatt, Nucl. Inst. Meth. **A 355**, 541 (1995).

Table 1: Measured cross-section ratios $\sigma_{\psi(2S)}/\sigma_{J/\psi(1S)}$: $R_{J/\psi\pi\pi}$ for the decay $\psi(2S) \rightarrow J/\psi(1S)\pi^+\pi^-$, $R_{\mu\mu}$ for the decay $\psi(2S) \rightarrow \mu^+\mu^-$, and R_{comb} for the two decay modes combined, for the kinematic range $5 < Q^2 < 80 \text{ GeV}^2$, $30 < W < 210 \text{ GeV}$ and $|t| < 1 \text{ GeV}^2$ at an ep centre-of-mass energy of 317 GeV . Also shown is $R_{\psi(2S)} = R_{J/\psi\pi\pi}/R_{\mu\mu}$. Statistical and systematic uncertainties are given.

$R_{J/\psi\pi\pi}$	$0.26 \pm 0.03^{+0.01}_{-0.01}$
$R_{\mu\mu}$	$0.24 \pm 0.05^{+0.02}_{-0.03}$
R_{comb}	$0.26 \pm 0.02^{+0.01}_{-0.01}$
$R_{\psi(2S)}$	$1.1 \pm 0.2^{+0.2}_{-0.1}$

Table 2: Measured cross-section ratios $\sigma_{\psi(2S)}/\sigma_{J/\psi(1S)}$: $R_{J/\psi\pi\pi}$ for the decay $\psi(2S) \rightarrow J/\psi(1S) \pi^+\pi^-$, $R_{\mu\mu}$ for the decay $\psi(2S) \rightarrow \mu^+\mu^-$, and R_{comb} for the two decay modes combined, as a function of Q^2 , W and $|t|$. Also shown is $R_{\psi(2S)} = R_{J/\psi\pi\pi}/R_{\mu\mu}$. The ratios as a function of W are measured in the range $5 < Q^2 < 80 \text{ GeV}^2$ and $|t| < 1 \text{ GeV}^2$, as a function of Q^2 in the range $30 < W < 210 \text{ GeV}$ and $|t| < 1 \text{ GeV}^2$, and as a function of $|t|$ in the range $5 < Q^2 < 80 \text{ GeV}^2$ and $30 < W < 210 \text{ GeV}$. All results are quoted for an ep centre-of-mass energy of 317 GeV , except for the bin $2 < Q^2 < 5 \text{ GeV}^2$, which refers to 300 GeV . Statistical and systematic uncertainties are given.

Q^2 (GeV ²)	$R_{J/\psi\pi\pi}$	$R_{\mu\mu}$	R_{comb}	$R_{\psi(2S)}$
2 – 5	$0.21 \pm 0.07^{+0.04}_{-0.03}$	$0.10 \pm 0.09^{+0.09}_{-0.09}$	$0.17 \pm 0.05^{+0.05}_{-0.02}$	–
5 – 8	$0.19 \pm 0.05^{+0.02}_{-0.02}$	$0.13 \pm 0.06^{+0.12}_{-0.03}$	$0.17 \pm 0.04^{+0.05}_{-0.02}$	$1.5 \pm 0.8^{+0.4}_{-0.7}$
8 – 12	$0.27 \pm 0.05^{+0.06}_{-0.01}$	$0.29 \pm 0.08^{+0.03}_{-0.08}$	$0.28 \pm 0.05^{+0.03}_{-0.03}$	$0.9 \pm 0.3^{+0.4}_{-0.1}$
12 – 24	$0.27 \pm 0.05^{+0.04}_{-0.03}$	$0.24 \pm 0.08^{+0.01}_{-0.08}$	$0.26 \pm 0.05^{+0.01}_{-0.03}$	$1.1 \pm 0.4^{+0.6}_{-0.1}$
24 – 80	$0.56 \pm 0.13^{+0.04}_{-0.09}$	$0.42 \pm 0.17^{+0.12}_{-0.04}$	$0.51 \pm 0.10^{+0.04}_{-0.04}$	$1.3 \pm 0.6^{+0.3}_{-0.6}$
W (GeV)	$R_{J/\psi\pi\pi}$	$R_{\mu\mu}$	R_{comb}	$R_{\psi(2S)}$
30 – 70	$0.24 \pm 0.07^{+0.01}_{-0.13}$	$0.24 \pm 0.10^{+0.03}_{-0.14}$	$0.24 \pm 0.06^{+0.01}_{-0.13}$	$1.0 \pm 0.5^{+0.5}_{-0.2}$
70 – 95	$0.30 \pm 0.06^{+0.01}_{-0.04}$	$0.31 \pm 0.09^{+0.09}_{-0.03}$	$0.30 \pm 0.05^{+0.02}_{-0.03}$	$1.0 \pm 0.3^{+0.1}_{-0.2}$
95 – 120	$0.28 \pm 0.06^{+0.05}_{-0.01}$	$0.24 \pm 0.08^{+0.04}_{-0.05}$	$0.27 \pm 0.05^{+0.03}_{-0.01}$	$1.2 \pm 0.5^{+0.5}_{-0.2}$
120 – 210	$0.22 \pm 0.05^{+0.07}_{-0.01}$	$0.17 \pm 0.07^{+0.02}_{-0.05}$	$0.21 \pm 0.04^{+0.03}_{-0.01}$	$1.3 \pm 0.6^{+0.7}_{-0.2}$
$ t $ (GeV ²)	$R_{J/\psi\pi\pi}$	$R_{\mu\mu}$	R_{comb}	$R_{\psi(2S)}$
0 – 0.1	$0.23 \pm 0.05^{+0.02}_{-0.02}$	$0.23 \pm 0.09^{+0.04}_{-0.05}$	$0.23 \pm 0.04^{+0.01}_{-0.02}$	$1.0 \pm 0.4^{+0.3}_{-0.2}$
0.1 – 0.2	$0.22 \pm 0.06^{+0.02}_{-0.03}$	$0.23 \pm 0.09^{+0.02}_{-0.06}$	$0.22 \pm 0.05^{+0.02}_{-0.02}$	$0.9 \pm 0.4^{+0.5}_{-0.2}$
0.2 – 0.4	$0.27 \pm 0.06^{+0.06}_{-0.01}$	$0.18 \pm 0.07^{+0.05}_{-0.06}$	$0.24 \pm 0.04^{+0.03}_{-0.02}$	$1.5 \pm 0.6^{+0.5}_{-0.2}$
0.4 – 1	$0.32 \pm 0.06^{+0.05}_{-0.03}$	$0.30 \pm 0.08^{+0.02}_{-0.05}$	$0.32 \pm 0.05^{+0.01}_{-0.02}$	$1.1 \pm 0.3^{+0.3}_{-0.1}$

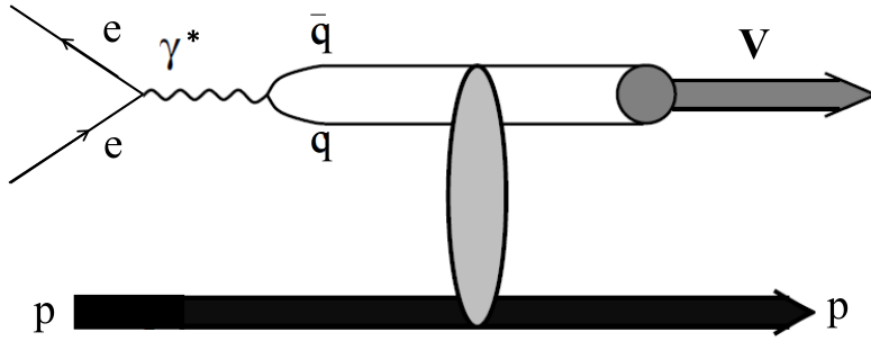


Figure 1: Schematic representation of the exclusive electroproduction of $q\bar{q}$ vector mesons. The electron emits a virtual photon, which fluctuates into a $q\bar{q}$ pair. The $q\bar{q}$ pair interacts with the target proton and produces the $q\bar{q}$ vector meson V .

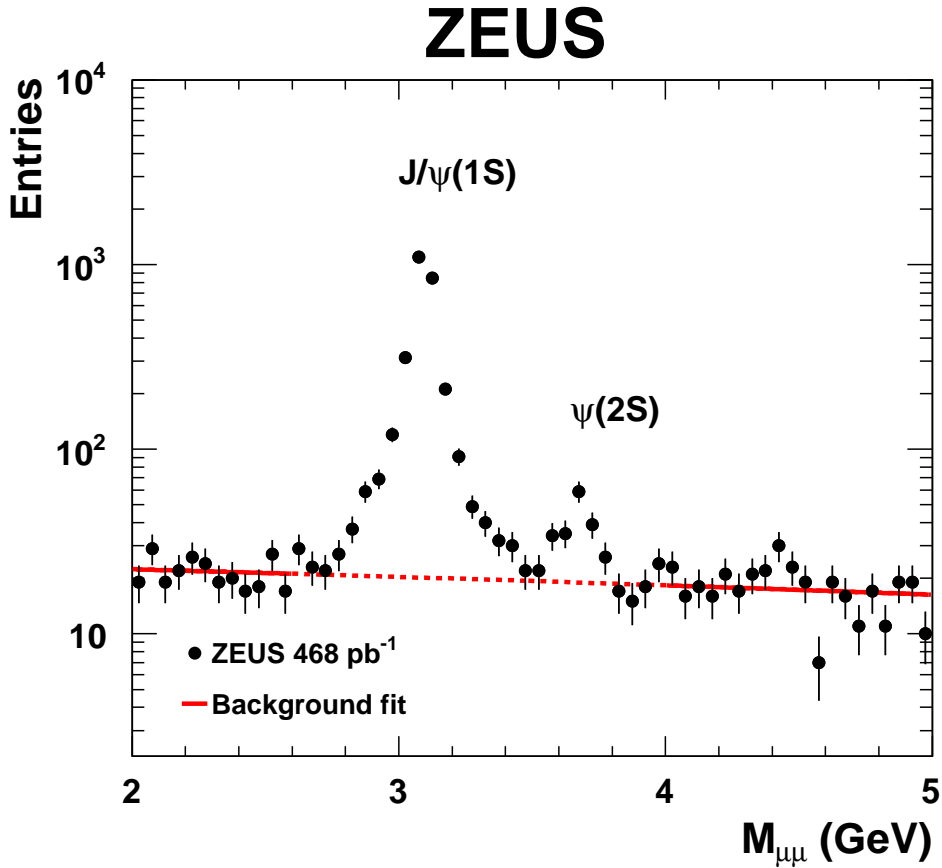


Figure 2: Two-muon invariant-mass distribution, $M_{\mu\mu}$, for exclusive dimuon events. The data (points) are shown with statistical uncertainties. The background distribution (solid line) is described by a linear fit to the data outside of the $J/\psi(1S)$ and $\psi(2S)$ signal regions, and is also shown (dashed line) in the signal regions.

ZEUS

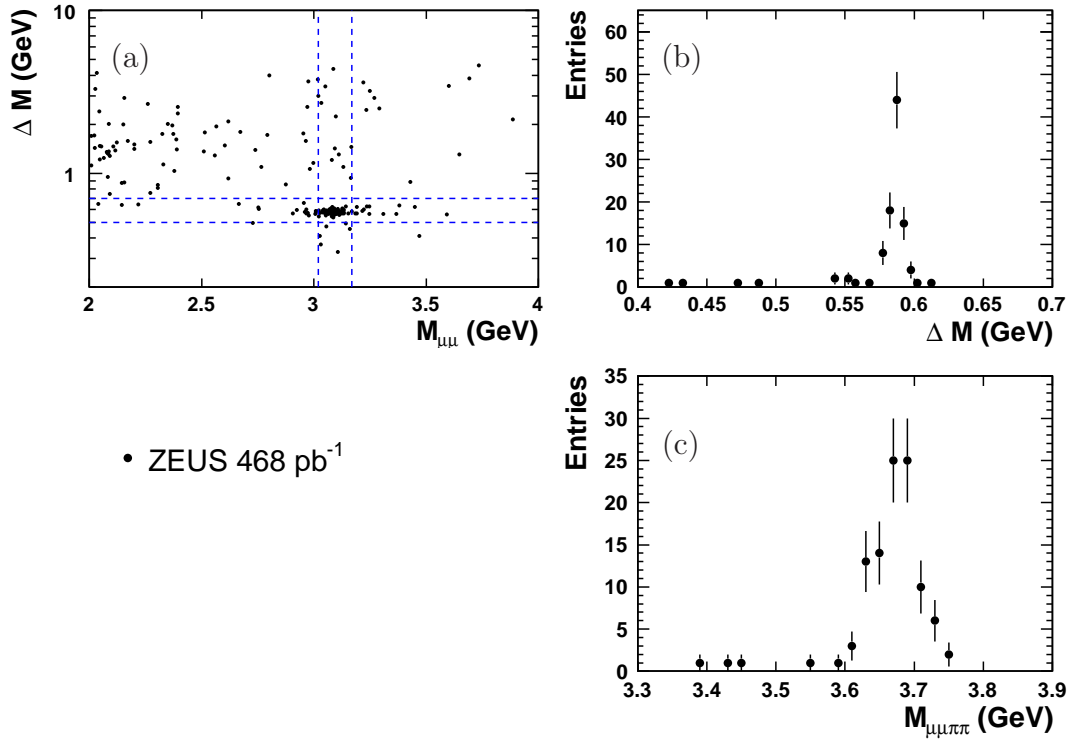


Figure 3: (a) Scatter plot of $\Delta M = M_{\mu\mu\pi\pi} - M_{\mu\mu}$ versus $M_{\mu\mu}$, for the selected $\mu\mu\pi\pi$ events, (b) ΔM distribution for $3.02 < M_{\mu\mu} < 3.17$ GeV and (c) $M_{\mu\mu\pi\pi}$ distribution for $3.02 < M_{\mu\mu} < 3.17$ GeV.

ZEUS

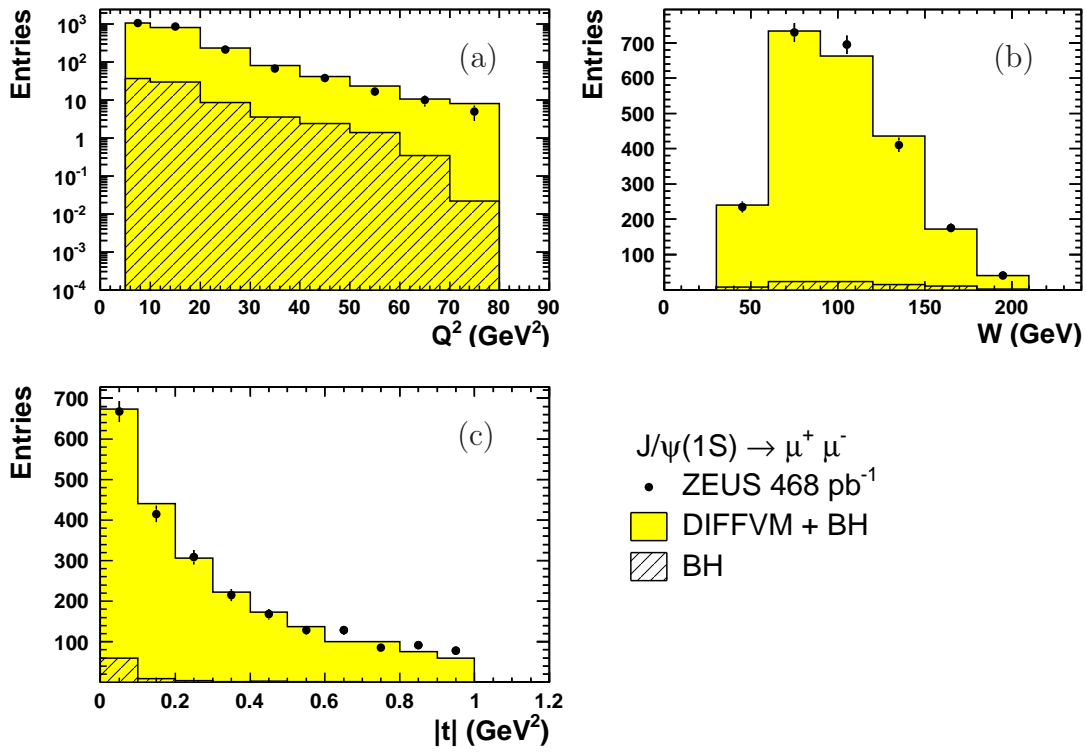


Figure 4: Comparison of the measured (points with statistical uncertainties) and the reweighted simulated distributions (shaded histograms) for the $J/\psi(1S) \rightarrow \mu^+ \mu^-$ events as a function of (a) Q^2 , (b) W and (c) $|t|$. The mass range $3.02 < M_{\mu\mu} < 3.17$ GeV was selected. The hatched histogram shows the contribution of the simulated Bethe–Heitler background.

ZEUS

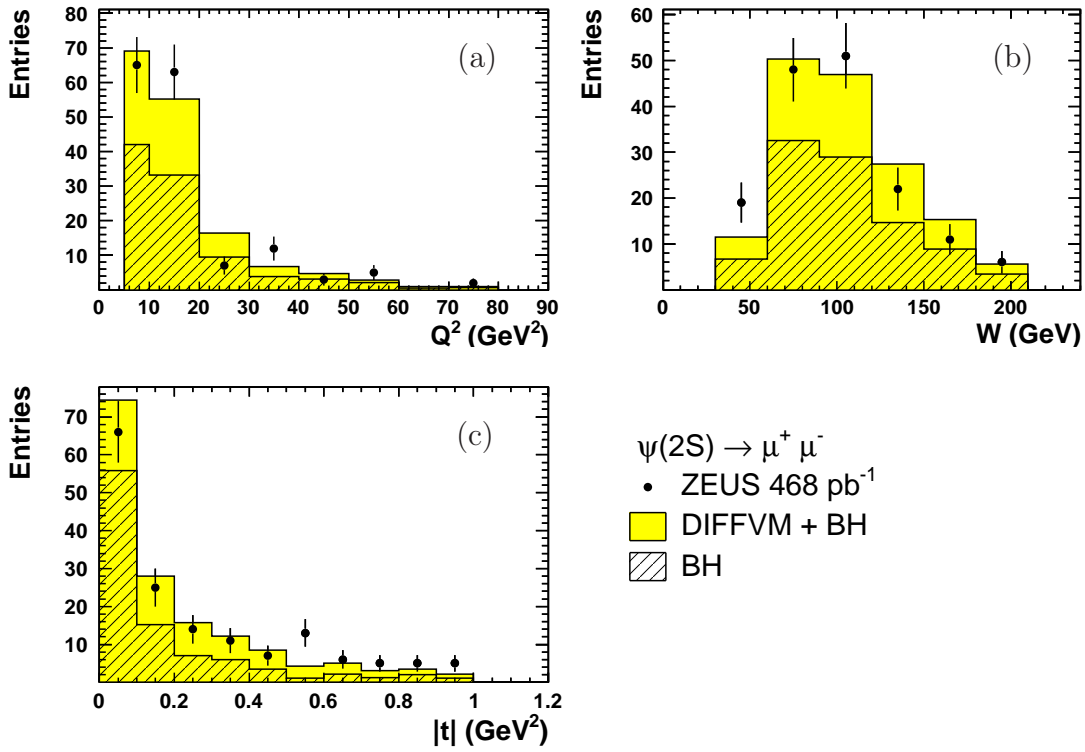


Figure 5: Comparison of the measured (points with statistical uncertainties) and the reweighted simulated distributions (shaded histograms) for the $\psi(2S) \rightarrow \mu^+ \mu^-$ events as a function of (a) Q^2 , (b) W and (c) $|t|$. The mass range $3.59 < M_{\mu\mu} < 3.79$ GeV was selected. The hatched histogram shows the contribution of the simulated Bethe–Heitler background.

ZEUS

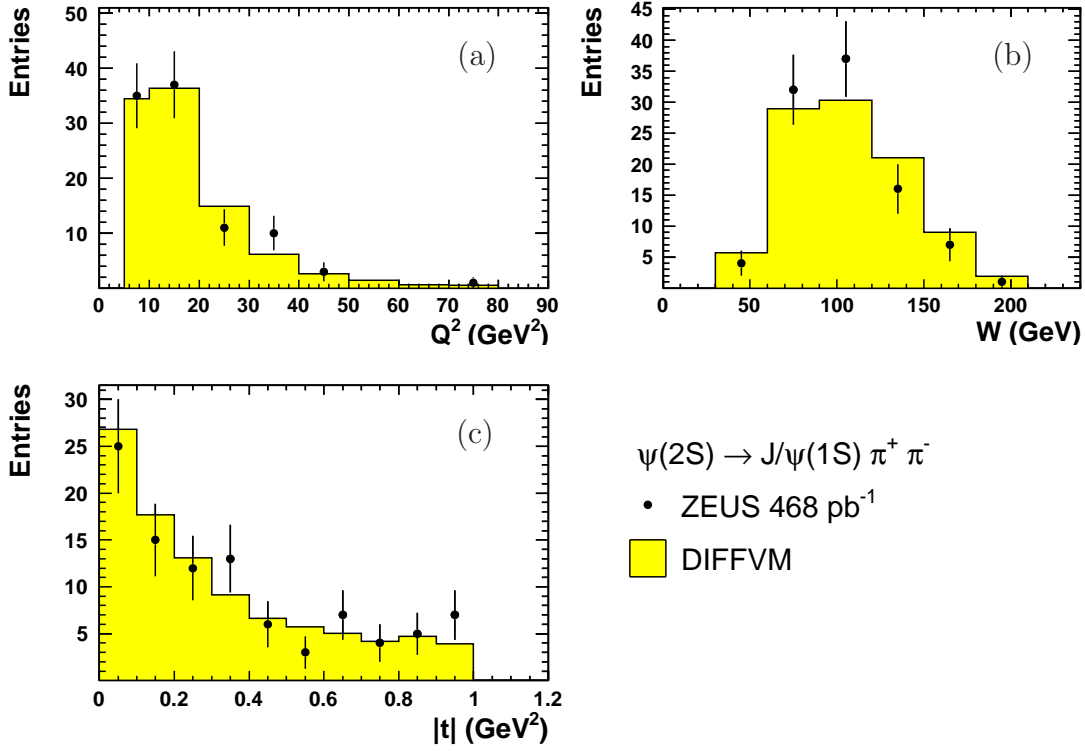


Figure 6: Comparison of the measured (points with statistical uncertainties) and the reweighted simulated distributions (shaded histograms) for the $\psi(2S) \rightarrow J/\psi(1S) \pi^+ \pi^-$ events as a function of (a) Q^2 , (b) W and (c) $|t|$. The mass ranges $3.02 < M_{\mu\mu} < 3.17$ GeV and $0.5 < \Delta M < 0.7$ GeV were selected.

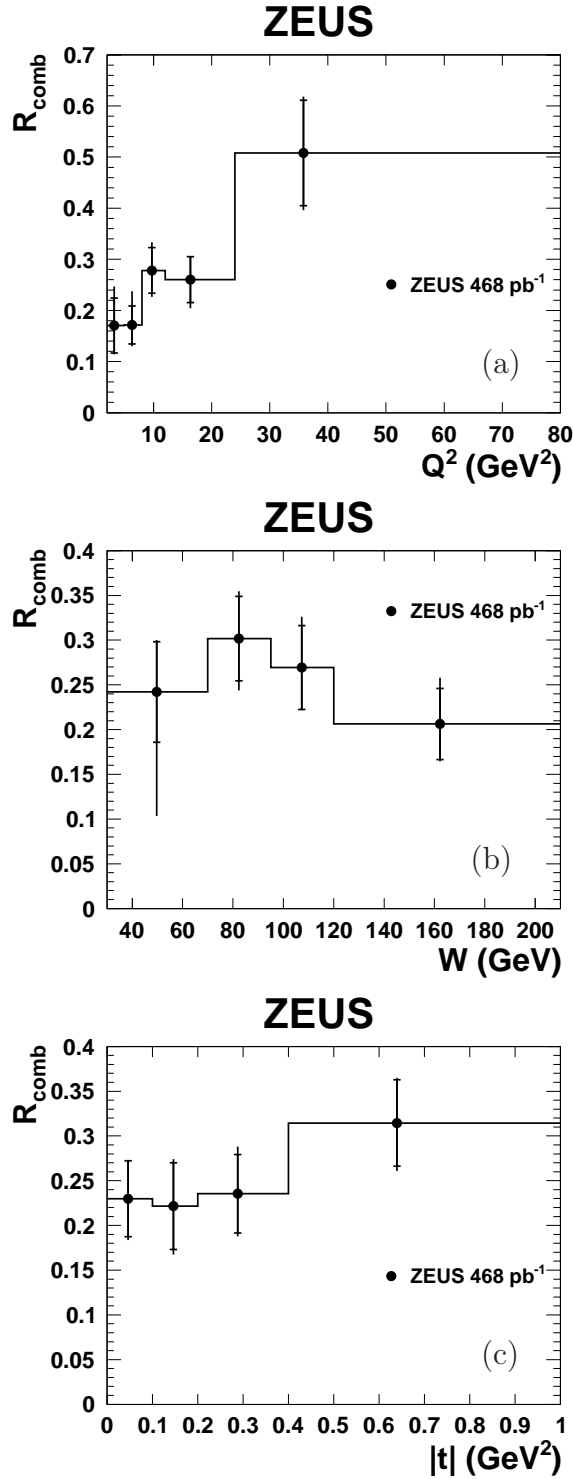


Figure 7: Cross-section ratio $R_{\text{comb}} = \sigma_{\psi(2S)}/\sigma_{J/\psi(1S)}$ for the combined $\psi(2S)$ decay modes as a function of (a) Q^2 , (b) W and (c) $|t|$. The horizontal lines show the bin widths, and the points are plotted at the average of the reweighted $\psi(2S)$ Monte Carlo events in the corresponding bin, as recommended elsewhere [52]. The inner error bars show the statistical and the outer error bars show the quadratic sum of statistical and systematic uncertainties.

ZEUS

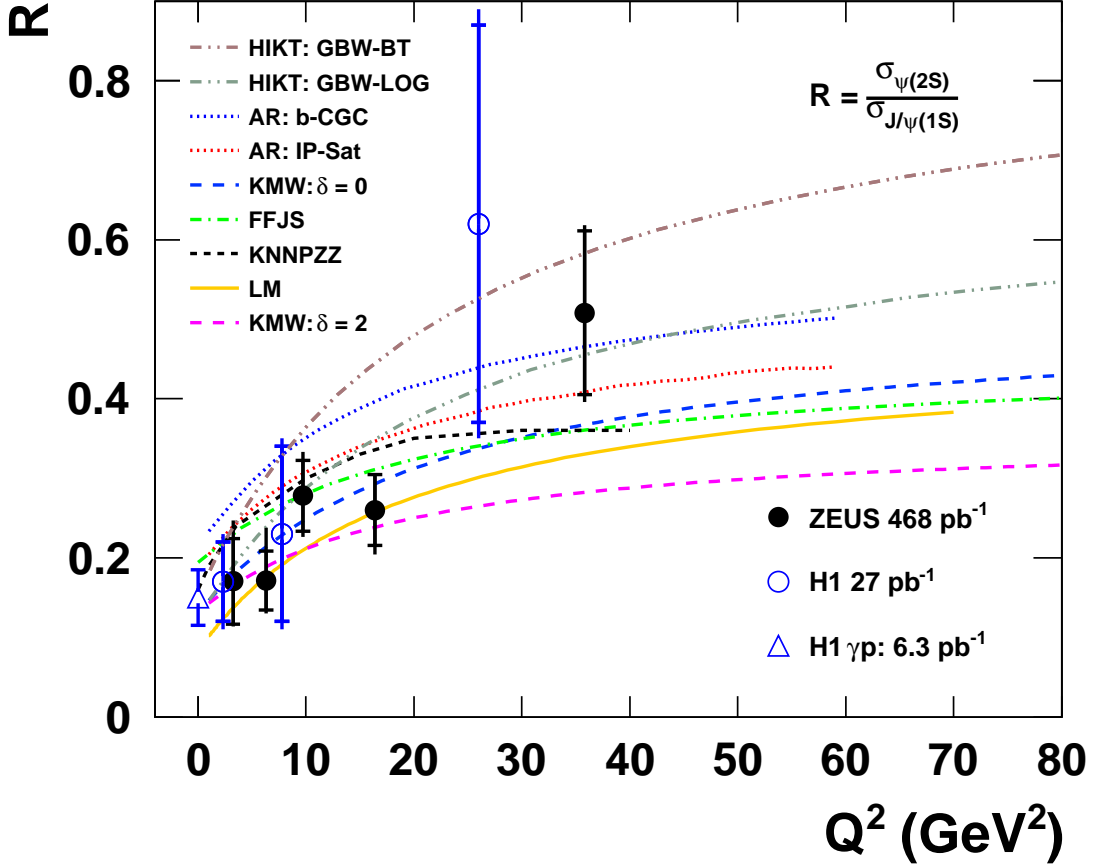


Figure 8: Cross-section ratio $R = \sigma_{\psi(2S)}/\sigma_{J/\psi(1S)}$ for the combined $\psi(2S)$ decay modes as a function of Q^2 . The kinematic range is $30 < W < 210$ GeV and $|t| < 1$ GeV² at an ep centre-of-mass energy of 317 GeV for the ZEUS data with $Q^2 > 5$ GeV² and 300 GeV for the ZEUS data with $2 < Q^2 < 5$ GeV². The ZEUS results (solid points) are shown compared to the previous H1 result (open points) [2] measured for $25 < W < 180$ GeV and $|t| < 1.6$ GeV² at an ep centre-of-mass energy of 300 GeV. The inner error bars show the statistical and the outer error bars show the quadratic sum of statistical and systematic uncertainties. The ZEUS points are plotted at the average Q^2 of the reweighted simulated $\psi(2S)$ events with the W and t cuts used in the analysis, as recommended elsewhere [52]. The model predictions discussed in Section 7.1 are shown as curves. The sequence of the labelling is in descending order of the R value at the highest Q^2 of each prediction.